Nanoscale

PAPER

View Article Online
View Journal | View Issue



Cite this: *Nanoscale*, 2020, **12**, 16113

# Realising the electrochemical stability of graphene: scalable synthesis of an ultra-durable platinum catalyst for the oxygen reduction reaction†

Gyen Ming A. Angel, [a] Noramalina Mansor,[a] Rhodri Jervis, [a] Zahra Rana,[a] Chris Gibbs,[a] Andrew Seel,[b] Alexander F. R. Kilpatrick, [c] Paul R. Shearing, [a] Christopher A. Howard, [b] Dan J. L. Brett *[a] and Patrick L. Cullen *[d]

Received 28th April 2020,
Accepted 27th June 2020

DOI: 10.1039/d0nr03326j

rsc.li/nanoscale

Creating effective and stable catalyst nanoparticle-coated electrodes that can withstand extensive cycling is a current roadblock in realising the potential of polymer electrolyte membrane fuel cells. Graphene has been proposed as an ideal electrode support material due to its corrosion resistance, high surface area and high conductivity. However, to date, graphene-based electrodes suffer from high defect concentrations and non-uniform nanoparticle coverage that negatively affects performance; moreover, production methods are difficult to scale. Herein we describe a scalable synthesis for Pt nanoparticle-coated graphene whereby $PtCl_2$ is reduced directly by negatively charged single layer graphene sheets in solution. The resultant nanoparticles are of optimal dimensions and can be uniformly dispersed, yielding high catalytic activity, remarkable stability, and showing a much smaller decrease in electrochemical surface area compared with an optimised commercial catalyst over 30 000 cycles. The stability is rationalised by identical location TEM which shows minimal nanoparticle agglomeration and no nanoparticle detachment.



## 1. Introduction

Satisfying global energy demands without damaging the environment is one of the great modern challenges. Using hydrogen in fuel cells provides a route to convert chemical into electrical energy with water as the only by-product at the point of use. Hydrogen fuel cells therefore provide a route to an efficient, environmentally-friendly, non-toxic electrochemical power source suitable for a wide range of applications.[1]

Of the many designs of fuel cells, the hydrogen fuelled polymer electrolyte membrane/proton exchange membrane (PEM) fuel cell is one of the most suitable for transport applications due to its fast start-up time, low temperature operation, solid electrolyte and favourable power-to-weight ratio. Currently, the most widely used catalyst for both the hydrogen oxidation reaction (HOR) at the anode and oxygen reduction reaction (ORR) at the cathode is platinum, or an alloy containing platinum.[1,2] The electrochemically active surface area per gram of metal can be maximised by creating platinum nanoparticles with optimized surface area-to-volume ratio. The ideal nanoparticle diameter for a fuel cell cathode is on the order of ~2 nm.[3] Smaller Pt nanoparticles possess more strain, leading to weaker $O_2$ binding and better ORR performance.[2] However, below 2 nm the higher proportion of low coordination number Pt atoms which bond strongly with $O_2$ leads to less catalytically active platinum,[3,4] moreover they readily agglomerate.[5–7]

In order to maximize Pt utilization, nanoparticles are typically decorated onto a porous carbon based support; this also promotes electronic connection and allows reactant gases to reach the catalyst. Catalyst durability is a significant challenge, especially when operating at low loading. Platinum nanoparticles degrade *via* various mechanisms across the 0.6–1 $V_{RHE}$ operating potential range, with carbon corrosion becoming more significant between 1–1.6 $V_{RHE}$.[4] Both of these potential ranges are directly relevant to fuel cell applications, where

[a]*Electrochemical Innovation Lab, Department of Chemical Engineering, University College London, Torrington Place, London WC1E 7JE, UK. E-mail: d.brett@ucl.ac.uk*
[b]*Department of Physics & Astronomy, University College London, London, WC1E 6BT, UK*
[c]*Institut für Chemie, Humboldt Universität zu Berlin, Brook-Taylor-Straße 2, 12489 Berlin, Germany*
[d]*School of Engineering and Materials Science (SEMS) and Material Research Institute, Queen Mary University of London, London, E1 4NS, UK. E-mail: p.cullen@qmul.ac.uk*

†Electronic supplementary information (ESI) available. See DOI: 10.1039/d0nr03326j

0.6–1 $V_{RHE}$ is typical of standard operating voltages, and 1–1.6 $V_{RHE}$ reflects the start-up and shut-down of the fuel cell.[8–10]

Graphene[11] has properties that could provide a high performance catalyst support[12] as it has high conductivity[13] and a very high surface area. Additionally, graphene has shown chemical resistance in acidic conditions.[14] However, the graphene used in the experiments which confirmed these properties was made by the non-scalable micromechanical cleavage or "scotch-tape" method. In order to exploit the properties of graphene on a larger scale much research effort has been dedicated to developing methods for the mass production of graphene.[15,16]

Liquid phase exfoliation of graphite provides a scalable graphene production method, and the liquids can then be used to efficiently cast the dispersed graphene sheets into working electrodes.[16] For producing a graphene-supported catalyst, by far the most common approach is *via* liquid-processable graphene oxide (GO) created from graphite using a modified Hummer's method.[17–26] High temperatures and/or aggressive chemicals are used to only partially reduce the non-conductive GO to conductive reduced graphene oxide rGO.[17–26] Finally, the rGO is then modified with the addition of metal nanoparticles. Unfortunately, the multiple energy intensive steps typically include ultracentrifugation and high temperatures, which are difficult to scale. Furthermore, the rGO contains a high number of defects which negatively impacts the electrode's durability,[9] especially at higher voltages associated with fuel cell start-up and shut-down (1–1.6 $V_{RHE}$). As a result, accelerated stress tests are typically only carried out across the 0.6–1 $V_{RHE}$ range, and rarely for more than a few thousand cycles to mitigate the damage that occurs over long cycles and higher loads. Table S1† presents a literature summary of accelerated stress test protocols and results. These generally fall far from the 30 000 cycle target set by the US DoE,[8,9,17] and rarely consider the 1–1.6 $V_{RHE}$ potential range.

An alternative strategy to exfoliate layered materials is to intercalate arrays of alkali metals between their layers and then dissolve the resulting compound in polar aprotic solvents.[27–30] These solutions can form spontaneously (*i.e.* without any agitation) with solutes comprising negatively charged 2D materials (termed graphenide in the case for negatively charged graphene) and positively charged cations. Graphenide solutions have been synthesised[29–32] using stage 1 graphite intercalation compounds (GICs), which have alkali metals between each graphene layer.[33] GICs such as $KC_8$ are known as precursors for metal-graphites[34] and it has been shown that the negative charge on the graphenide can be used to reduce some metal salts to form metal particles (Mn, Zn, Cu) on a 10–200 nm scale.[35] More recently this has also been achieved for metal and metal oxide nanoparticles.[32,36,37]

In this work, for the first time, uniformly-sized Pt nanoparticles have been grown on a low-defect graphene support in a scalable, one-pot synthesis. This is achieved by reacting graphenide solutions with $PtCl_2$. It has been shown that using a low and controlled alkali metal : graphene ratio, produces stable, extremely well dispersed Pt nanoparticles of ideal dimensions for PEM fuel cell catalysis. The graphenide-derived platinum nanoparticle/graphene hybrid (GD-Pt/G) is shown to catalyse ORR, with a performance that matches that of a state-of-the-art commercial Pt/C catalyst. Furthermore, GD-Pt/G exhibits excellent durability compared to the commercial Pt/C catalyst across both 0.6–1 $V_{RHE}$ and 1–1.6 $V_{RHE}$ potential range accelerated stress tests. The accelerated stress tests are in line with DoE protocols and are conducted over many more cycles than comparable literature (see Table S1†).

## 2. Experimental section

### 2.1 Production of charged graphene dispersion

Graphite (~325 mesh, Sigma) was evacuated down to a pressure of $10^{-6}$ mbar and outgassed at 400 °C until base pressure was achieved. This was then loaded into an argon glove box ($H_2O$ < 0.1 ppm, $O_2$ < 0.1 ppm) and placed in a sealed reaction vessel with potassium metal (Sigma, 99.95%) at a K : C ratio of 1 : 24. This reaction vessel was then placed onto a high integrity gas manifold and evacuated to $10^{-6}$ mbar. Anhydrous $NH_3$ was condensed onto the reaction vessel at −60 °C until the characteristic deep-blue colour[38] of the dilute (<1 moles percent metal, *i.e.* <1 moles K for 99 moles $NH_3$) metal-ammonia solution was seen. When the liquid turned colourless, indicating that intercalation had been completed, the $NH_3$ was cryopumped from the sample, leaving a light blue powder[39] of $KC_{24}(NH_3)_{1.3}$ graphite intercalation compound (GIC). Previous $C^{13}$ NMR studies of these GICs have shown that there is only one C atom environment, as expected from an unfunctionalised eclipsed stacking arrangement of the C layers with electrons donated from the metal to the graphite, delocalised.[40] This metal-ammonia GIC was then transferred to a glove box where THF was added at a concentration of 5 mg $ml^{-1}$. In order to increase the concentration of the negatively charged graphene platelets in a timely manner, bath sonication was applied, in a method previously reported.[29] The resultant solutions were allowed to settle in the glove box for a further 24 hours before the supernatant was separated from undispersed powder for use.

### 2.2 Production of $PtCl_2$ dispersion

$PtCl_2$ was added to THF inside the glove box at a concentration of 1 mg $ml^{-1}$. This was then sonicated for 30 minutes, keeping the temperature below 30 °C.

### 2.3 Reaction of graphene dispersion with $PtCl_2$

In the glovebox, the $PtCl_2$ dispersion was added to the charged graphene liquid in a stoichiometric amount, assuming a 100% yield of GIC to graphenide production and a reaction where 2 moles of potassium are required to reduce 1 mole of $PtCl_2$. As undispersed GIC powder remained in the bottle the supernatant was taken from, this results in an excess of $PtCl_2$. This was left to react under gentle stirring overnight.

### 2.4 TEM

Once the GD-Pt/G hybrid was synthesized in THF, it was drop-cast onto a holey carbon grid. For identical location TEM, gold mesh "finder" grids were used. TEM was then performed on a Jeol JEM 2100 equipped with a $LaB_6$ source.

### 2.5 Rotating disk electrochemistry

A 40 μl aliquot of GD-Pt/G ink was dropped onto a polished ($Al_2O_3$ micro-polish, Bueler) 0.1963 $cm^2$ glassy carbon electrode, achieving a loading of ~10 $\mu g_{Pt}$ $cm^{-2}$. Subsequently 8 μl of 0.02 wt% Nafion ionomer solution was added to the surface of the electrode, serving as a binder. This was used with a standard three-electrode cell, containing 0.1 M $HClO_4$ electrolyte solution, a reversible hydrogen electrode (Gaskatel) and a Pt mesh counter electrode. For the commercial Pt/C (Johnson Matthey HiSpec4000), 1 mg of the catalyst was dispersed in 1 ml of 0.05 wt% Nafion in 75%/25% water/IPA mixture. A loading of 35 $\mu g_{Pt}$ $cm^{-2}$ was deposited onto the glassy carbon electrode. The $PtCl_2$ ink control sample was produced by adding $PtCl_2$/THF dispersion to an amount of THF equivalent to the volume of graphenide solution used in the preparation of GD-Pt/G (in total 0.62 mg $ml^{-1}$). The electrode was then prepared following the same procedure as used for the GD-Pt/G ink, providing a control sample with the same amount of $PtCl_2$ on the electrode, that would have been on the GD-Pt/G electrode if there had been no reaction with graphenide. Working electrodes were first electrochemically activated *via* rapid cycling (500 mV $s^{-1}$, 50 cycles) between 0.05 $V_{RHE}$ and 1.2 $V_{RHE}$. Cyclic voltammograms were obtained by cycling the working electrode between 0.025 $V_{RHE}$ and 1.2 $V_{RHE}$ at room temperature, under $N_2$ flow, at a scan rate of 20 mV $s^{-1}$.

In order to investigate ORR activity, linear sweep voltammetry was performed at room temperature under constant $O_2$ flow at 1600 rpm. The scans were performed at 20 mV $s^{-1}$ between −0.01 $V_{RHE}$ and 1 $V_{RHE}$.

To examine the durability of the platinum nanoparticles and the graphene support, corrosion experiments were carried out across both 0.6–1 $V_{RHE}$ and 1–1.6 $V_{RHE}$ ranges. Here, the working electrode was cycled at 100 mV $s^{-1}$, and then at various intervals, a full CV was taken between 0.025 $V_{RHE}$ and 1.2 $V_{RHE}$ at 20 mV $s^{-1}$ in order to obtain the ECSA.[41] 30 000 cycles were carried out for each durability test.

### 2.6 Image processing

Using Gwyddion software, Fig. 2(b) was thresholded to only select the Pt nanoparticles, making it possible to determine the co-ordinates of every detected nanoparticle centre and measure the distances between each centre. This information was used to create the radial distribution function shown in Fig. 2(d), with the average number density calculated by number of detected particles in an area of known size (754 nanoparticles in 66 651 $nm^2$).

## 3. Results and discussion

The charged graphene dispersion was synthesised *via* the "metal-ammonia" method, which can produce exclusively single layer graphenide as previously reported[29] and is described in detail in the Methods section. The solutions are stable due to the charge on the graphene. The process for making the GD-Pt/G material is shown schematically in Fig. 1. The reaction occurs when platinum(II) chloride dispersed in THF is added to the dispersion of negatively charged graphene sheets in THF. Once the reaction is complete the graphene is uncharged, and as a result the material flocculates,[31] with platinum nanoparticles separating the individualised graphene sheets. The restacked structure can be seen in Fig. S1,† where a platinum-covered graphene sheet is disturbed by the transmission electron microscope (TEM) beam. This causes one sheet to slide across another, revealing more of the underlying sheet, which is also decorated with platinum nanoparticles. This is further supported by Raman spectroscopy of GD-Pt/G shown in Fig. S2.†

The 2D peak can be fitted with a single Lorentzian centred on *ca.* 2700 $cm^{-1}$, with a FWHM of *ca.* 67 $cm^{-1}$, suggesting a turbostratic restacking of graphene.[42] Furthermore, the $I(D)/I(G)$ is 0.33 which is significantly lower than the $I(D)/I(G)$ reported for rGO supports,[20,22,43,44] suggesting GD-Pt/G is less defective. Fig. 2 presents TEM micrographs of GD-Pt/G, obtained *via* the reaction of sonication-aided dissolution of $KC_{24}(NH_3)_{1.3}$ with $PtCl_2$. The resultant material consists of ~micron-sized layered structures covered uniformly with a high density of nanometre sized objects. Fig. 2(a) shows a close up image of a GD-Pt/G sheet. Analysis of the lattice planes, shown in Fig. S3,† confirms the nanoparticles to be metallic Pt as expected, with the (111) planes of the Pt nanoparticles marked on the micrograph. This suggests that the Pt nanoparticles are formed by the on-sheet reduction of $PtCl_2$ by the delocalised charge present on the graphene sheets.

By manually measuring 1034 nanoparticles in Fig. 2(a), the particle diameter distribution displayed in Fig. 2(c) has been obtained. The histogram is well-fitted by a Gaussian function from which the mean diameter of the Pt was calculated to be (1.7 ± 0.6) nm. By stitching together many nanometre-resolution micrographs (Methods), it was possible to produce a composite TEM micrograph, allowing for the high resolution required to distinguish individual nanoparticles to be realised across a much larger area (*ca.* 1 $\mu m^2$). Fig. 2(b) demonstrates the homogeneity of the distribution of the nanoparticles on the graphene surface, with very few examples of agglomerate particles. The distribution of the nanoparticles was investigated by calculating the Pt–Pt site-centre, site-centre radial distribution function, $g(r)$, of the Pt nanoparticles (Fig. 2(d), Methods). The $g(r)$ demonstrates the Pt particles are well ordered with respect to one another. The distribution has a clear peak at 2.5 nm, corresponding to the average inter-particle nearest neighbour distance, and a smaller second peak at 4.75 nm. As well as the size of the particles, the edge-to-edge distance between nanoparticles makes a significant difference

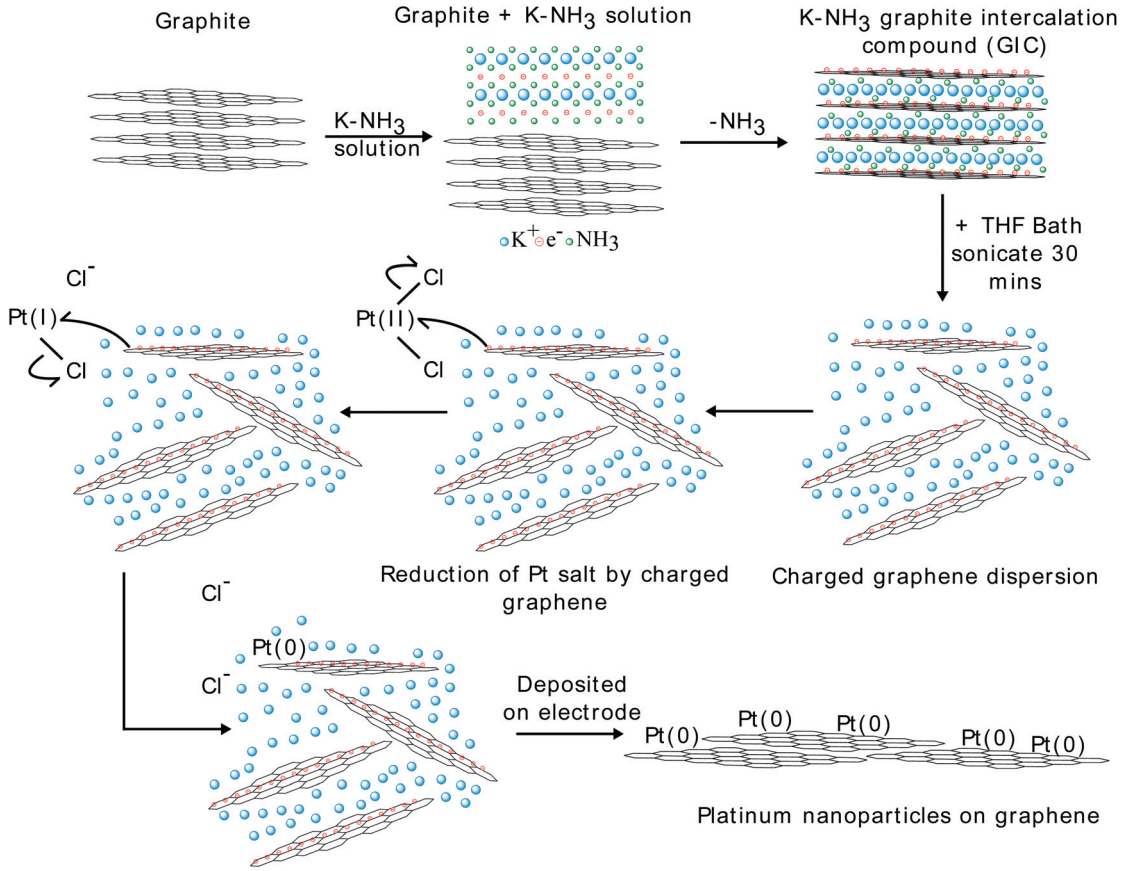


**Fig. 1** Reaction scheme for the reduction of $PtCl_2$ by graphenide to produce Pt(0) particles on graphene.

in catalytic activity, with a significant increase in specific activity as the separation decreases below 1 nm.[45] With an average edge-to-edge distance of 0.8 nm, this proximity effect may contribute to GD-Pt/G's strong electrocatalytic performance (as discussed in the results shown below).

Rotating disk electrode experiments were carried out to investigate the performance of the GD-Pt/G as a catalyst for ORR. Cyclic voltammetry was used to calculate the electrochemical surface area (ECSA) of a GD-Pt/G sample, a commercial Pt/carbon sample and a $PtCl_2$ control sample (Fig. S4†). The hydrogen adsorption and desorption regions of the CV for GD-Pt/G show no distinct peaks, suggesting the broad peaks observed are a convolution of the peaks associated with the crystal facets of platinum and that the nanoparticles are polycrystalline.[46] Using X-ray photoelectron spectroscopy (XPS), a typical GD-Pt/G sample was found to be 11.5 wt% platinum, with a corresponding RDE loading weight of 10.3 $\mu g_{Pt}$ $cm^{-2}$ (Fig. S5†). The ECSA of GD-Pt/G was found to be 94.40 $m^2$ $g_{pt}^{-1}$, which compares favourably with the ECSA of Pt/carbon, 58.21 $m^2$ $g_{pt}^{-1}$. The high ECSA can be attributed to the fine distribution of platinum nanoparticles in GD-Pt/G. The $PtCl_2$ control sample, with an ECSA of 0.29 $m^2$ $g_{pt}^{-1}$, shows that any contribution to excess $PtCl_2$ of catalytic activity, when compared to GD-Pt/G, is negligible (Fig. S4†). Furthermore, there are no features of platinum in the $PtCl_2$ CV, only double layer capacitance.

Fig. 3 presents the linear sweep voltammograms and associated Tafel plots obtained for GD-Pt/G and commercial Pt/C electrodes, measured at a rotation rate of 1600 rpm in 0.1 M $HClO_4$, with a scan rate of 20 mV $s^{-1}$ in accordance to DOE protocols adapted for RDE (See ESI†).

In Fig. 3(a) it can be seen that the GD-Pt/G electrode closely matches the onset and half-wave potentials and limiting current of the highly-optimised commercial Pt/C electrode. Specific and mass activities were calculated from the kinetic current, obtained from the current measured at 0.9 $V_{RHE}$.[41] Although specific activities were found to be similar (465 and 413 μA $cm_{Pt}^{-2}$ for GD-Pt/G and Pt/C respectively), the mass activity of GD-Pt/G was approximately twice as large as of the commercial sample, as shown in Table 1. The observed increased mass activity suggests that the graphene support improves the utilisation of the available platinum nanoparticles, likely due its facilitation of the formation of well-dispersed Pt nanoparticles, and its high conductivity.[37,47,48]

The Tafel plots displayed in Fig. 3(b) were obtained from Fig. 3(a) by calculating mass-transport corrected kinetic current densities and plotting them against potential. The associated Tafel slopes were estimated to be 56 mV $dec^{-1}$ for

 

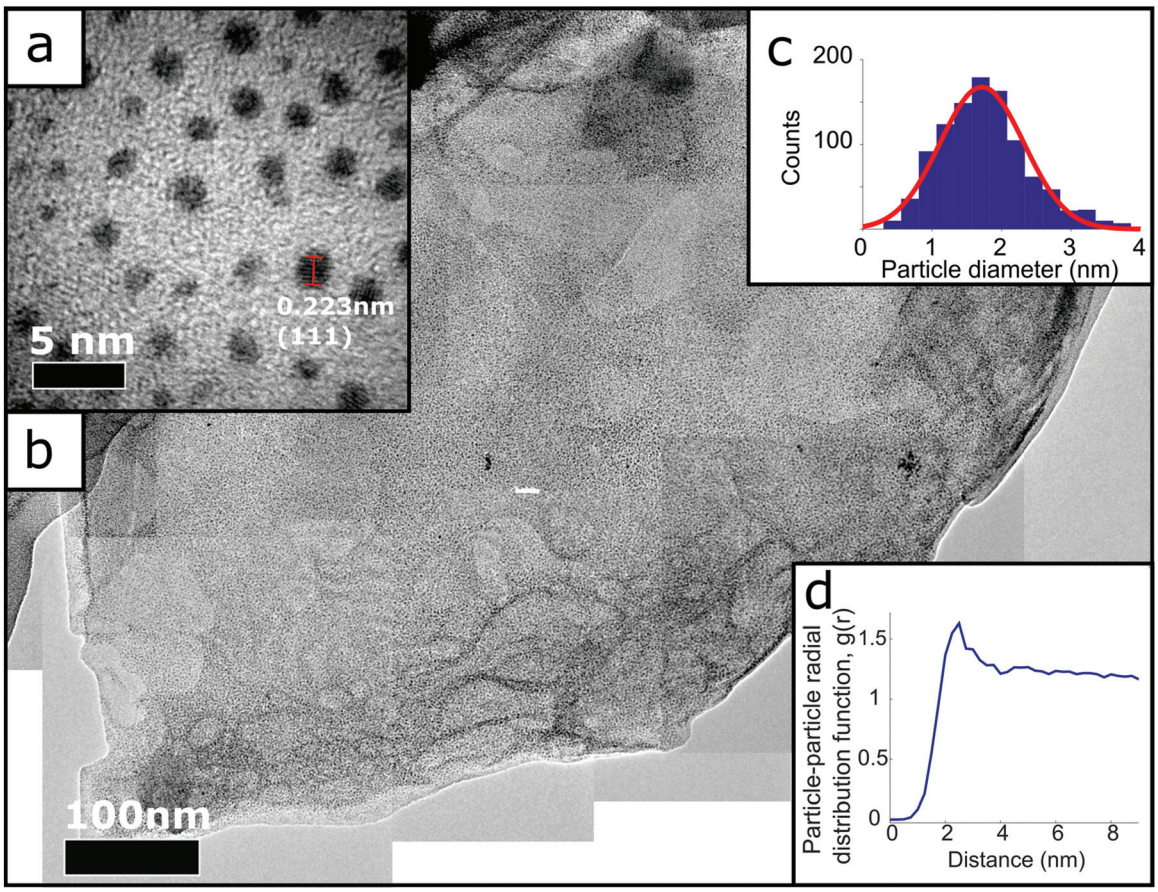


**Fig. 2** (a) Single transmission electron micrograph of the same sheet exhibited in (b) showing the (111) distance of a platinum nanoparticle. (b) Composite transmission electron micrograph of a graphene sheet decorated with Pt nanoparticles. (c) A histogram of 100 nanoparticle diameters measured manually from (a), fit with a Gaussian. (d) Radial distribution function, $g(r)$, calculated using centres of particles detected using image processing software (Methods).

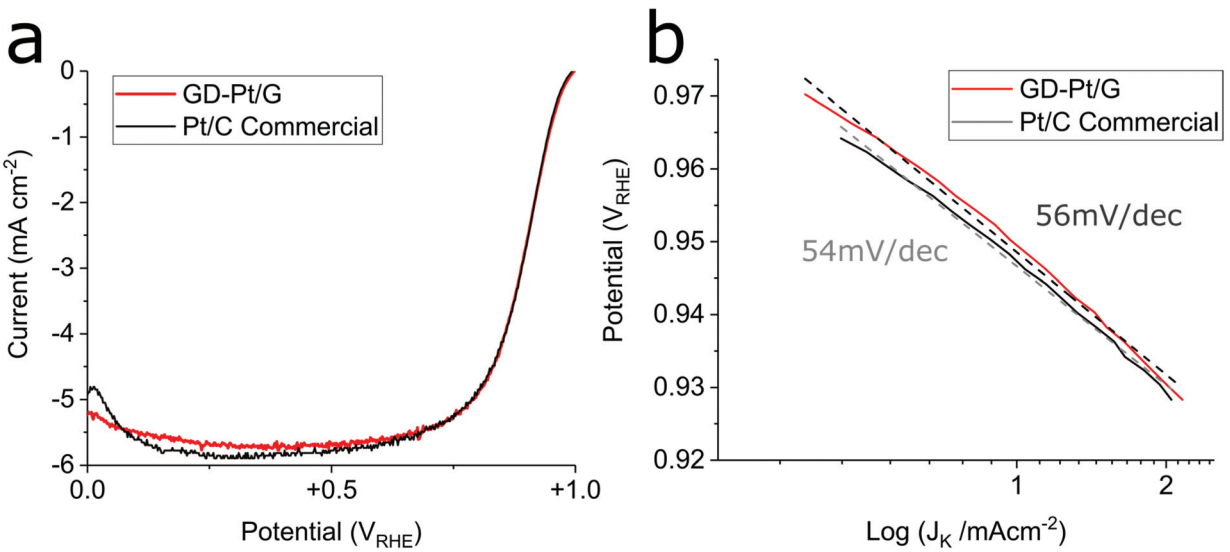


**Fig. 3** (a) Linear sweep voltammograms for ORR in $O_2$ saturted 0.1 M $HClO_4$, comparing the activity of GD-Pt/G with a commercial Pt/C catalyst, rotation rate 1600 rpm, scan rate 20 mV $s^{-1}$. (b) Tafel plots derived from 3(a) for ORR on GD-Pt/G and Pt/C electrodes.

**Table 1** Summary of electrochemical surface area, specific activity and mass activity of GD-Pt/G compared with a commercial Pt/C catalyst

| Material | ECSA ($m^2\ g_{pt}^{-1}$) | Specific activity ($\mu A\ cm_{Pt}^{-2}$) | Mass activity ($A\ mg_{pt}^{-1}$) |
|---|---|---|---|
| GD-Pt/G | 94.0 | 465 | 0.44 |
| Pt/C | 54.8 | 413 | 0.23 |

GD-Pt/G, and 54 mV $dec^{-1}$ for commercial Pt/C. These values suggest that for both catalysts, the ORR proceeds *via* the preferred 4-electron pathway, for which the coverage of the adsorbed oxygen intermediates is the rate limiting factor.[1,49,50] The ORR mechanism is further evidenced by rotating ring-disk electrode experiments, in which the number of electrons transferred was found to be above 3.9 across the entirety of the

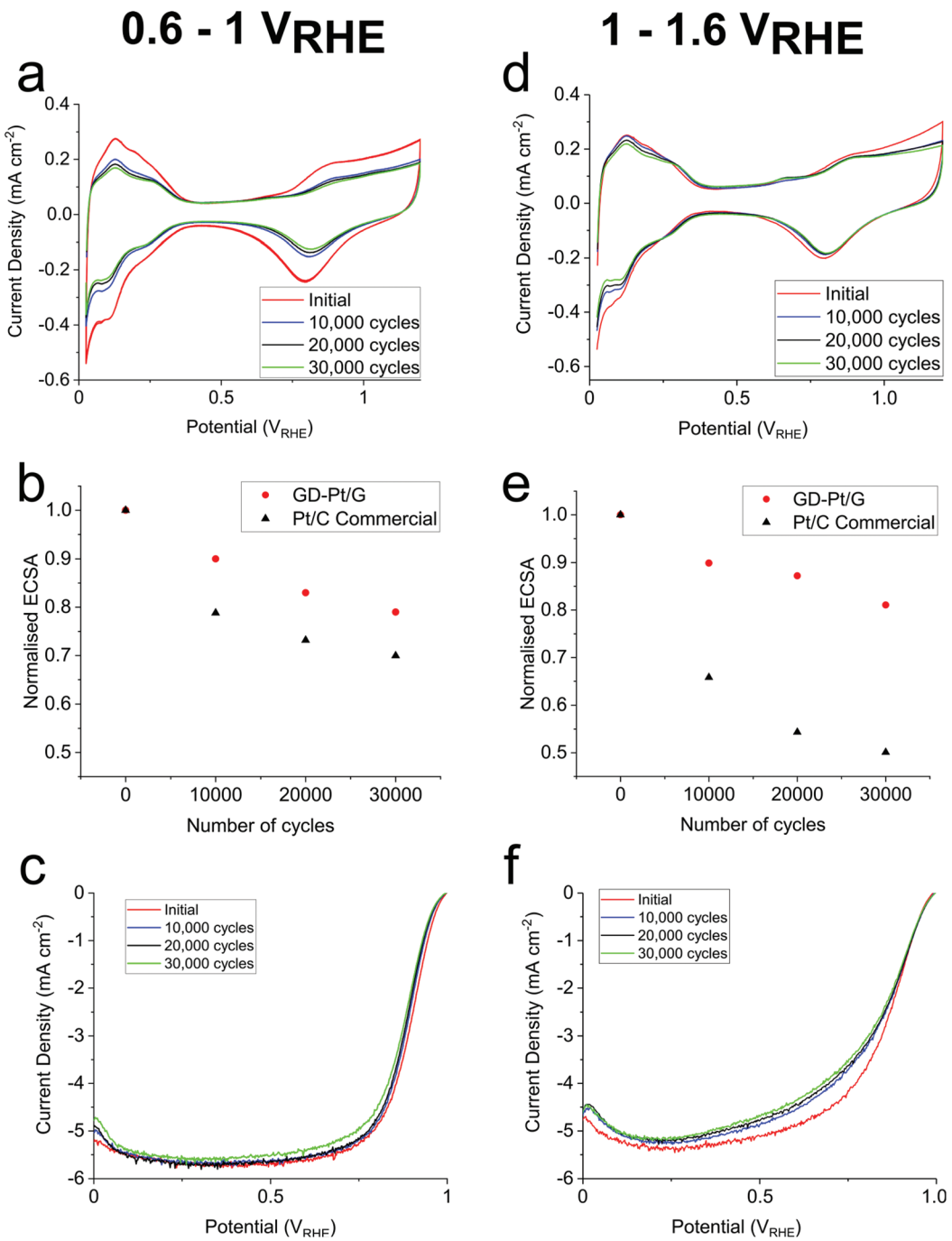


**Fig. 4** (a) Cyclic voltammograms for GD-Pt/G measured across the 0.6–1 $V_{RHE}$ accelerated stress test, with associated normalised change in electrochemical surface area, compared with Pt/C, and polarisation curves shown in (b) and (c) respectively. (d) Cyclic voltammograms for GD-Pt/G measured across the 1–1.6 $V_{RHE}$ accelerated stress test, with associated normalised change in electrochemical surface area, compared with Pt/C, and polarisation curves shown in (e) and (f) respectively.

potential range, and the percentage of $H_2O_2$ produced remained below 1% (Fig. S6 and S7†). To assess the durability of the GD-Pt/G catalyst, accelerated stress tests were carried out for 30 000 cycles between both 0.6–1 $V_{RHE}$ and 1–1.6 $V_{RHE}$ based on DoE accelerated stress tests (see ESI†). The cyclic voltammograms, the ORR polarisation curves and the associated relative change in the normalised electrochemical surface areas (ECSAs), are shown in Fig. 4. Fig. 4(a) and (d) show the cyclic voltammograms measured for GD-Pt/G at 10 000 cycle intervals, from which the hydrogen adsorption peaks (0.075–0.4 $V_{RHE}$) were used to calculate the ECSAs.

The ECSA values were then normalised to the initial ECSA and plotted against the number of accelerated stress test cycles, presented in Fig. 4(b) and (e). From these figures, it can be seen that, across the 30 000 cycles, the ECSA of commercial Pt/C sample degraded by as much as 30% and 50% during the 0.6–1 $V_{RHE}$ and 1–1.6 $V_{RHE}$, tests respectively. Meanwhile, GD-Pt/G maintained its activity remarkably well, showing a comparatively small ECSA loss of 21% and 19% for the same number of cycles. The stability is further reflected in the ORR polarisation curves shown in Fig. 4(c) and (f), which show negligible change in the onset potentials, and very little change in half-wave potentials and limiting currents after 30 000 cycles (Table S2†).

These results show our GD-Pt/G material show best in class durability when compared to any platinum graphene based ORR catalyst reported in the literature as summarised in Table S1.† Upon cycling, the decrease in catalytic activity in typical Pt/C catalysts is due to the corrosion of the carbon and the change in distribution of the platinum within the system.

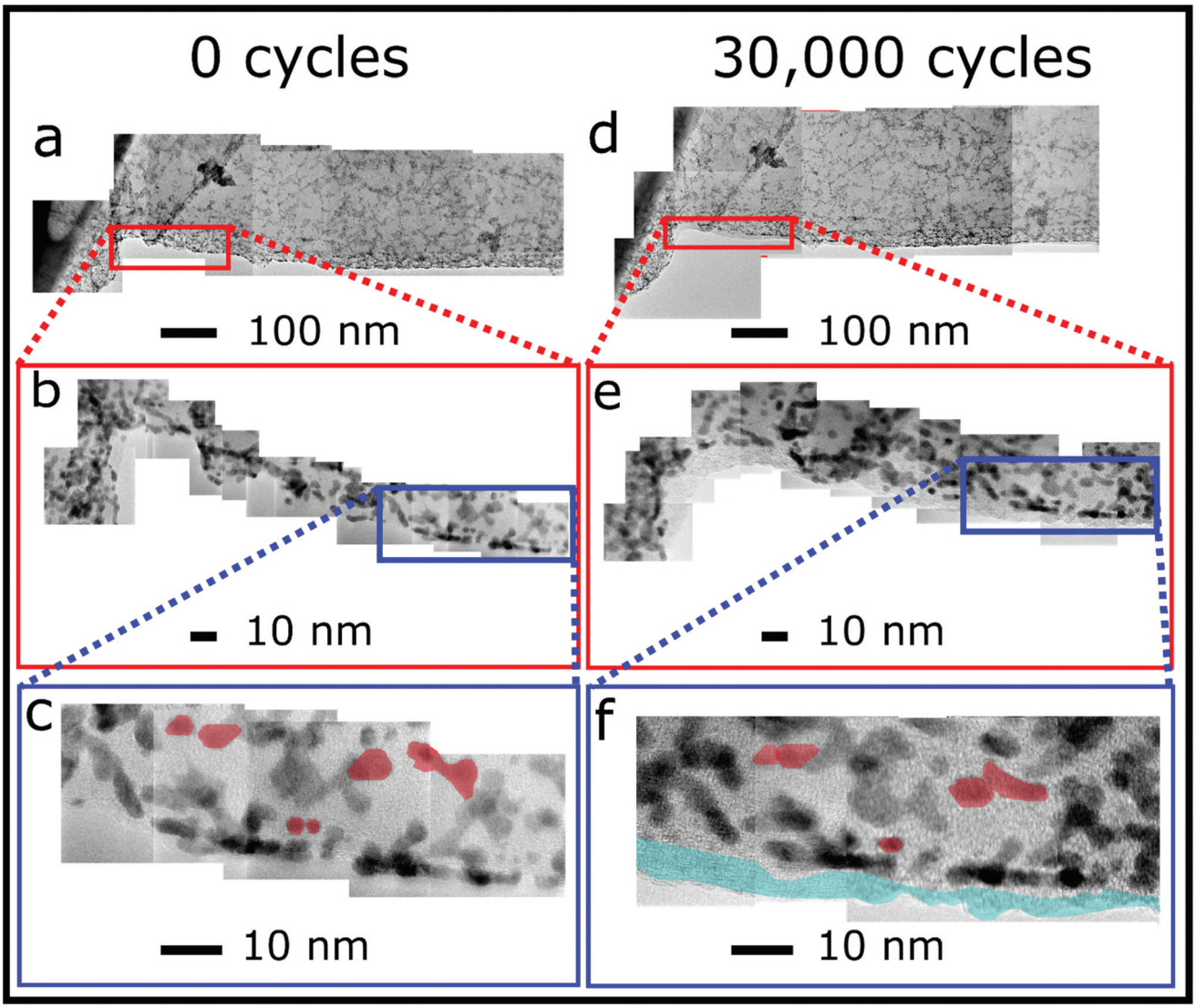


**Fig. 5** Identical location TEM images at varying length scales. (a) and (d) show a micron length stitch before and after corrosion, respectively. (b) and (e) correspond to the highlighted red boxes in (a) and (c), showing an area two hundred nanometres across, built-up of atomic resolution images. (c) and (f) correspond to the highlighted blue boxes in (b) and (e), where examples of nanoparticle migration and agglomeration are highlighted in red and the added Nafion layer shown blue.

Suggested mechanisms for these changes are: size increase of platinum nanoparticles *via* 3D Ostwald ripening, migration/agglomeration of platinum nanoparticles, platinum dissolution into the electrolyte and the detachment of platinum nanoparticles from the carbon support due to carbon corrosion.[5–7]

The effects of these mechanisms can be observed using identical location TEM (ILTEM), which offers the unique ability to image the same area of material before and after cycling, where the TEM grid is directly used as the working electrode.[7] To further investigate the durability of GD-Pt/G, ILTEM was performed to give a qualitative assessment of which corrosion mechanisms were responsible for activity loss. Gold ILTEM grids were prepared *via* drop-casting GD-Pt/G ink and examined before and after 30 000 0.6–1 $V_{RHE}$ potential cycles. Fig. 5 shows composite TEM micrograph stitches of the same area of a sample of overlapping sheets of GD-Pt/G at various length scales, before and after the accelerated stress test. Fig. 5(a) and (d) present *ca.* 1 μm length of material. At this resolution, it can be seen that the GD-Pt/G remains almost completely unchanged, showing clear resistance to the typical corrosion mechanisms seen in commercial Pt/C catalysts.[7] The structure of the nanoparticle distribution appears to be unaffected by the cycling: in order to find any differences it is necessary to evaluate the sample at much higher resolutions. The areas shown in the red rectangles in Fig. 5(a) and (d), are shown at a higher resolution in Fig. 5(b) and (e), respectively. The sections in blue are then shown at an even higher resolution in Fig. 5(c) and (f), where the composites are built from atomic resolution micrographs. At this resolution, it is possible to observe small changes in the distribution of the nanoparticles. In Fig. 5(c) and (f), examples of platinum nanoparticles agglomerating have been highlighted in red. As these particles can be seen to have moved small distances to agglomerate, it appears that this has occurred *via* the migration mechanism rather than *via* Ostwald ripening. Importantly, there are no distinguishable cases of nanoparticle detachment. The blue area along the edge of the graphene sheet shown in Fig. 5(f) highlights the presence of the Nafion added as part of the accelerated stress test. The changes in platinum nanoparticle distribution and graphene sheets shown in Fig. 5 are much less significant than what is typically observed with commercial Pt/C catalysts,[7] where extensive nanoparticle agglomeration and loss of up to half of the nanoparticles can be observed in as few as 4 hours of cycling.[51] This is consistent with the small relative decrease in the activity of the GD-Pt/G catalyst. In the majority of methods, nanoparticles are formed *via* reduction of a platinum precursor by a secondary reducing agent and interact with the supporting material *via* van der Waals force. Previous studies[32,37] have suggested that the distribution of nanoparticles is due to the limited supply of charge available to reduce the platinum precursor. By making use of the metal-ammonia method to intercalate graphite, it has been possible to obtain a stage 1 GIC ($KC_{24}(NH_3)_{1.3}$) in which the graphene sheets have lower charge density than for the typical stage 1 compound $KC_8$.[32,37] The lower charge ratio may explain the production of smaller nanoparticles, well-suited for electrocatalysis.

The stability of the platinum nanoparticles on GD-Pt/G can be attributed to the direct reduction of the $PtCl_2$ by the negatively charged graphene sheets, which anchors the nanoparticles to them directly, as suggested by Hof *et al.*[32,52] The improved durability of the graphene across the 1–1.6 $V_{RHE}$ accelerated stress test compared with carbon and other reduced graphene oxide supported catalysts is likely due to the method with which the graphene is produced. This results in graphene with a low number of defects, meaning there are fewer sites for the initiation of carbon corrosion.[52,53]

## 4. Conclusion

In summary, a scalable method that directly makes use of charged graphene sheets to reduce $PtCl_2$ has been used to produce high quality graphene decorated with well-dispersed platinum nanoparticles (GD-Pt/G). GD-Pt/G has been shown to exhibit excellent activity toward the ORR, closely matching the performance and mechanism of a highly-optimised commercial Pt/C catalyst. Furthermore, GD-Pt/G demonstrates very high stability, showing much smaller relative decreases in electrochemical surface area and performance than commercial Pt/C across a much larger number of cycles than previously reported in the literature. Transmission electron microscopy has been used to characterise the nanoparticle distribution across large surface areas. Using identical location TEM, it has been shown that the relatively small changes in activity post-cycling may be attributed to the excellent durability of the graphene sheets, low levels of agglomeration and lack of detachment of platinum nanoparticles. As a result, it is expected that GD-Pt/G is suitable for scale up for use in membrane electrode assemblies within fuel cells and electrolysers. As a general synthesis method this has the potential to produce different metal nanoparticles finely dispersed across graphene which could be tailored for electrochemical applications across the fields of catalysis, sensors and supercapacitors.

## Author contributions

The manuscript was written through contributions of all authors. All authors have given approval to the final version of the manuscript. PLC conceived the project with RJ. PLC and DJB directed the project. TEM was performed by PLC and GMAA. RDE, Raman spectroscopy and accelerated stress tests were performed by GMAA. PLC and GMAA wrote the paper.

## Conflicts of interest

Some of the authors have filed a patent application based on the preparation of this material (WO/2019/158569). There are no other conflicts of interest.

## Acknowledgements

PLC would like to thank the EPSRC for funding this project: EP/M506448/1, EP/S001298/1.

## References

1 O. T. Holton and J. W. Stevenson, *Platinum Met. Rev.*, 2013, **57**, 259–271.
2 S. Guo, S. Zhang and S. Sun, *Angew. Chem., Int. Ed.*, 2013, **52**, 8526–8544.
3 M. Shao, A. Peles and K. Shoemaker, *Nano Lett.*, 2011, **11**, 3714–3719.
4 D. Y. Chung, J. M. Yoo and Y. E. Sung, *Adv. Mater.*, 2018, **30**, 1704123.
5 Y. Shao, G. Yin and Y. Gao, *J. Power Sources*, 2007, **171**, 558–566.
6 L. Dubau, L. Castanheira, G. Berthomé and F. Maillard, *Electrochim. Acta*, 2013, **110**, 273–281.
7 M. Arenz and A. Zana, *Nano Energy*, 2016, **29**, 299–313.
8 A. Riese, D. Banham, S. Ye and X. Sun, *J. Electrochem. Soc.*, 2015, **162**, F783–F788.
9 J. Speder, A. Zana, I. Spanos, J. J. K. Kirkensgaard, K. Mortensen, M. Hanzlik and M. Arenz, *J. Power Sources*, 2014, **261**, 14–22.
10 H. A. Gasteiger, S. S. Kocha, B. Sompalli and F. T. Wagner, *Appl. Catal., B*, 2005, **56**, 9–35.
11 K. S. Novoselov, A. K. Geim, S. V. Morozov, D. Jiang, Y. Zhang, S. V. Dubonos, I. V. Grigorieva and A. A. Firsov, *Science*, 2004, **306**, 666–669.
12 N. M. Julkapli and S. Bagheri, *Int. J. Hydrogen Energy*, 2015, **40**, 948–979.
13 M. Liu, R. Zhang and W. Chen, *Chem. Rev.*, 2014, **114**, 5117–5160.
14 S. Böhm, *Nat. Nanotechnol.*, 2014, **9**, 741–742.
15 L. Banszerus, M. Schmitz, S. Engels, M. Goldsche, K. Watanabe, T. Taniguchi, B. Beschoten and C. Stampfer, *Nano Lett.*, 2016, **16**, 1387–1391.
16 J. N. Coleman, M. Lotya, A. O'Neill, S. D. Bergin, P. J. King, U. Khan, K. Young, A. Gaucher, S. De, R. J. Smith, I. V. Shvets, S. K. Arora, G. Stanton, H. Y. Kim, K. Lee, G. T. Kim, G. S. Duesberg, T. Hallam, J. J. Boland, J. J. Wang, J. F. Donegan, J. C. Grunlan, G. Moriarty, A. Shmeliov, R. J. Nicholls, J. M. Perkins, E. M. Grieveson, K. Theuwissen, D. W. McComb, P. D. Nellist and V. Nicolosi, *Science*, 2011, **331**, 568–571.
17 J. Liu, Q. Ma, Z. Huang, G. Liu and H. Zhang, *Adv. Mater.*, 2019, **1800696**, 1800696.
18 R. Kou, Y. Shao, D. Wang, M. H. Engelhard, J. H. Kwak, J. Wang, V. V. Viswanathan, C. Wang, Y. Lin, Y. Wang, I. A. Aksay and J. Liu, *Electrochem. Commun.*, 2009, **11**, 954–957.
19 H. Yin, H. Tang, D. Wang, Y. Gao and Z. Tang, *ACS Nano*, 2012, **6**, 8288–8297.
20 Y.-X. Huang, J.-F. Xie, X. Zhang, L. Xiong and H.-Q. Yu, *ACS Appl. Mater. Interfaces*, 2014, **6**, 15795–15801.
21 L. Sun, H. Wang, K. Eid, S. M. Alshehri, V. Malgras, Y. Yamauchi and L. Wang, *Electrochim. Acta*, 2016, **188**, 845–851.
22 Y. Zheng, S. Zhao, S. Liu, H. Yin, Y. Y. Chen, J. Bao, M. Han and Z. Dai, *ACS Appl. Mater. Interfaces*, 2015, **7**, 5347–5357.
23 S. Xu and P. Wu, *J. Mater. Chem. A*, 2014, **2**, 13682–13690.
24 P. Zhang, W. Tu, R. Wang, S. Cai, J. Wu, Q. Yan, H. Pan, H. Zhang and H. Tang, *Int. J. Electrochem. Sci.*, 2016, **11**, 10763–10778.
25 X. Mu, Z. Xu, Y. Ma, Y. Xie, H. Mi and J. Ma, *Electrochim. Acta*, 2017, **253**, 171–177.
26 M. Wojnicki, M. Luty-Blocho, K. Mech, J. Grzonka, K. Fitzner and K. J. Kurzydlowski, *J. Flow Chem.*, 2015, **5**, 22–30.
27 C. Vallés, C. Drummond, H. Saadaoui, C. a. Furtado, M. He, O. Roubeau, L. Ortolani, M. Monthioux and A. Pénicaud, *J. Am. Chem. Soc.*, 2008, 1–4.
28 K. Huang, G. Delport, L. Orcin-Chaix, C. Drummond, J. S. Lauret and A. Pénicaud, *Nanoscale*, 2016, **8**, 8810–8818.
29 E. M. Milner, N. T. Skipper, C. A. Howard, M. S. P. Shaffer, D. J. Buckley, K. A. Rahnejat, P. L. Cullen, R. K. Heenan, P. Lindner and R. Schweins, *J. Am. Chem. Soc.*, 2012, **134**, 8302–8305.
30 P. L. Cullen, K. M. Cox, M. K. Bin Subhan, L. Picco, O. D. Payton, D. J. Buckley, T. S. Miller, S. A. Hodge, N. T. Skipper, V. Tileli and C. A. Howard, *Nat. Chem.*, 2017, **9**, 244–249.
31 A. Catheline, C. Vallés, C. Drummond, L. Ortolani, V. Morandi, M. Marcaccio, M. Iurlo, F. Paolucci and A. Pénicaud, *Chem. Commun.*, 2011, **47**, 5470–5472.
32 F. Hof and A. Pénicaud, *Chem. – Eur. J.*, 2018, **24**, 16246–16250.
33 M. S. Dresselhaus and G. Dresselhaus, *Adv. Phys.,* 2002, **511**, 1–186.
34 D. Savioa, C. Trombini and A. Umani-Ronchi, *Pure Appl. Chem.*, 1985, **57**, 1887–1896.
35 S. A. Hodge, H. H. Tay, D. B. Anthony, R. Menzel, D. J. Buckley, P. L. Cullen, N. T. Skipper, C. A. Howard and M. S. P. Shaffer, *Faraday Discuss.*, 2014, **172**, 311–325.
36 E. G. C. Neiva, V. H. R. Souza, K. Huang, A. Pénicaud and A. J. G. Zarbin, *J. Colloid Interface Sci.*, 2015, **453**, 28–35.
37 F. Hof, A. Boni, G. Valenti, K. Huang, F. Paolucci and A. Pénicaud, *Chem. – Eur. J.*, 2017, **23**, 15283–15288.
38 M. T. J. H. Lodge, P. Cullen, N. H. Rees, N. Spencer, K. Maeda, J. R. Harmer, M. O. Jones and P. P. Edwards, *J. Phys. Chem. B*, 2013, **117**, 13322–13334.
39 B. R. York and S. A. Solin, *Phys. Rev. B: Condens. Matter Mater. Phys.*, 1985, **31**, 8206–8220.
40 T. Tsang, R. M. Fronko, H. A. Resing, X. W. Qian and S. A. Solin, *Solid State Commun.*, 1987, **62**, 117–120.
41 Y. Garsany, O. A. Baturina, K. E. Swider-Lyons and S. S. Kocha, *Anal. Chem.*, 2010, **82**, 6321–6328.
42 L. M. Malard, M. A. Pimenta, G. Dresselhaus and M. S. Dresselhaus, *Phys. Rep.*, 2009, **473**, 51–87.

43 B. Sravani, P. Raghavendra, Y. Chandrasekhar, Y. Veera Manohara Reddy, R. Sivasubramanian, K. Venkateswarlu, G. Madhavi and L. Subramanyam Sarma, *Int. J. Hydrogen Energy*, 2020, **45**, 7680–7690.
44 Y. Kim, D. Lee, Y. Kwon, T. W. Kim, K. Kim and H. J. Kim, *J. Electroanal. Chem.*, 2019, **838**, 89–93.
45 M. Nesselberger, M. Roefzaad, R. F. Hamou, P. U. Biedermann, F. F. Schweinberger, S. Kunz, K. Schloegl, G. K. H. Wiberg, S. Ashton, U. Heiz, K. J. J. Mayrhofer and M. Arenz, *Nat. Mater.*, 2013, **12**, 919–924.
46 K. Yamamoto, D. M. Kolb, R. Kötz and G. Lehmpfuhl, *J. Electroanal. Chem.*, 1979, **96**, 233–239.
47 E. Antolini, *Appl. Catal., B*, 2012, **123–124**, 52–68.
48 F. Hof, M. Liu, G. Valenti, E. Picheau, F. Paolucci and A. Pénicaud, *J. Phys. Chem. C*, 2019, **123**, 20774–20780.
49 K. Wang, H. Wang, S. Ji, H. Feng, V. Linkov and R. Wang, *RSC Adv.*, 2013, **3**, 12039.
50 T. Shinagawa, A. T. Garcia-esparza and K. Takanabe, *Sci. Rep.*, 2015, **5**, 13081.
51 K. J. J. Mayrhofer, J. C. Meier, S. J. Ashton, G. K. H. Wiberg, F. Kraus, M. Hanzlik and M. Arenz, *Electrochem. Commun.*, 2008, **10**, 1144–1147.
52 E. Bertin, A. Münzer, S. Reichenberger, R. Streubel, T. Vinnay, H. Wiggers, C. Schulz, S. Barcikowski and G. Marzun, *Appl. Surf. Sci.*, 2019, **467–468**, 1181–1186.
53 Y. Shao, S. Zhang, C. Wang, Z. Nie, J. Liu, Y. Wang and Y. Lin, *J. Power Sources*, 2010, **195**, 4600–4605.